

1 Introduction

Amid the rapid advancement of global digitalization, 5G communication technology has progressively reached widespread commercial deployment. Nevertheless, its performance in critical parameters — such as data transmission rate (with a current peak of approximately 20 Gbps), regional traffic density [around 0.01 Gbit/(s·m²)], and latency (approximately 1 millisecond) — is increasingly insufficient to meet the stringent requirements of a future intelligent society characterized by the internet of everything and the necessity for real-time interaction. Against this backdrop, the research and development of 6G communication technology has become the focus of global technological competition. The International Telecommunication Union (ITU) and research institutions from various countries (such as the European Union's Hexa-X and the United States' Next G Alliance) have clearly stated that the core goal of 6G is to achieve “integrated space-air-ground-ocean coverage”. This coverage will support ultra-high data rates (1 Tbps level), ultra-dense regional traffic [1 Gbit/(s·m²) level], ultra-low latency (0.1 ms level), and full-spectrum communication spanning terahertz to visible light [1–3]. The terahertz (THz) band (0.1–10 THz) is recognized as the “golden frequency band” for 6G due to its unique spectral characteristics. Nevertheless, the practical application of terahertz technology relies on high-performance terahertz detectors — their sensitivity, response speed, noise level, and integration degree directly determine the overall performance of terahertz systems. Therefore, developing terahertz detectors that operate at room temperature, with high sensitivity, low noise, and easy integration is a core challenge for the industrialization of 6G communication and terahertz technology [4]. The development history of terahertz detectors can be traced back to the late 20th century. Early research mainly focused on thermal detectors (such as Golay cells and bolometers). These detectors operate on the principle of absorbing terahertz energy to induce temperature changes, and then converting this energy into electrical signals [5]. Although thermal detectors have a simple structure and low cost, their slow response speed and low sensitivity make them unable to meet the needs of high-speed communication.

Since the 21st century, breakthroughs in semiconductor technology and nanomaterials have driven quantum detectors (based on the photoelectric effect) to gradually become mainstream. These detectors can achieve picosecond-level response speeds, and their sensitivity has been significantly improved. However, they still face challenges such as the requirement for low-temperature operation and complex manufacturing processes. The following review summarizes domestic and international research progress from three perspectives: material systems, structural design, and integration technology.

Early terahertz detectors were primarily based on III–V semiconductors (such as GaAs and InSb) and operated by exploiting free carrier absorption or the photoconductive effect [6]. For example, in the early 1990s, Dyakonov and Shur's pioneering theoretical work predicted that steady-state current flow in a field-effect transistor (FET) channel could become unstable due to plasma wave generation — these waves can emit electromagnetic radiation at the plasma wave frequency. In early experiments, submicron GaAs and GaN FETs were observed to emit terahertz radiation (nanowatt-level power) at both low and room temperatures [7]. Kun *et al.* [8] successfully demonstrated a photoconductive terahertz detector based on a single GaAs/AlGaAs/GaAs core-shell-cap nanowire. This detector operates effectively in the 0.1–0.6 THz range, with performance attributed to a simple double-pad antenna that achieves local field enhancement. After further optimizing the antenna design, a single InP nanowire photoconductive detector exhibited high-amplitude, phase-sensitive time-domain spectroscopy across a 0.1–2 THz broadband range [8]. In recent years, ternary alloy Weyl semimetals (such as MoWTe₂) have attracted significant research interest due to their unique phase transition characteristics. Previously, mechanically exfoliated black phosphorus was demonstrated to act as a saturable absorber for erbium-doped fiber lasers, enabling passive Q-switching and mode-locking operations [9]. As a room-temperature-stable Weyl semimetal, MoWTe₂ exhibits both a narrow photoluminescence bandwidth and high carrier mobility — giving it superior potential for terahertz detection applications. MoWTe₂ is formed by combining MoTe₂ and WTe₂. Unlike MoTe₂ (which requires temperature-induced phase transitions) and WTe₂ (which has a short Fermi arc), MoWTe₂ can stably exist in the Weyl semimetal phase at room temperature. Additionally, its photoluminescence intensity varies noticeably with increasing thickness, with single-layer MoWTe₂ showing high photoluminescence intensity [10–12]. These properties suggest its potential application in optoelectronic devices, such as high-resolution optical displays and high-sensitivity photodetectors. Domestic research on the terahertz-related properties of 2D layered materials has also made significant progress. Cheng *et al.* [13] systematically studied the terahertz optical conductivity and electronic relaxation dynamics of 2H-stacked bilayer MoS₂ using terahertz time-domain spectroscopy.

Traditional terahertz detectors mainly adopt planar structures, where terahertz waves interact with the active layer only at the surface — leading to low energy utilization efficiency. To enhance light–matter interaction, the design of micro- and nanostructures has become crucial. Similar to the CRISPR/Cas12a-enabled surface plasmon resonance (SPR) platform (which achieves highly sensitive detection through technological integration [14]), this study uses 3D microstructures to

excite the LSP effect. It applies the local field enhancement mechanism in the terahertz band, effectively improving the interaction efficiency between MoWTe₂ and terahertz waves. Surface plasmon polariton (SPP) and LSP effects can confine terahertz fields to subwavelength scales, significantly improving absorption efficiency. For example, antimonene-based SPR sensors achieve ultrasensitive detection by leveraging the strong interaction between the material and molecules [15]. In this study, the combination of MoWTe₂ and the LSP effect of 3D microstructures further enhances field localization — thus increasing the detector's R_a and reducing its NEP. Lin *et al.* [16] designed a 3D bow-shaped microarray terahertz detector using projection microstereolithography (P μ SL) technology. This detector combines the LSP effect of non-microcavity structures with the exceptional properties of Weyl semimetal materials. Its photoresponsivity at 0.1 THz increased from 0.30 MV/W to 0.54 MV/W, while NEP decreased from 92 pW/Hz^{1/2} to 50 pW/Hz^{1/2} — confirming the effectiveness of the LSP effect [16]. Additionally, Guo *et al.* [17] integrated graphene with an asymmetric butterfly antenna. It utilized the LSP effect to enhance terahertz wave absorption in graphene, thereby improving detector photoresponsivity. The maximum photoresponsivity of this detector reaches 19.6 V/W at 2.52 THz, with an NEP of 0.59 nW/Hz^{1/2} — demonstrating the performance enhancement brought by microstructures [17].

The fabrication of conventional micro-nano structures generally depends on electron beam lithography (EBL) or focused ion beam (FIB) techniques, both of which entail intricate procedures and substantial expenses. The advancement of 3D printing technology offers a novel approach for fabricating microstructures. For example, detectors based on β -InSe exhibit excellent polarization-sensitive characteristics due to their low-symmetry crystal structure [18]. The 3D rotating rectangular array designed in this study breaks C_6 symmetry — this not only enhances terahertz absorption but also provides a structural reference for the future development of terahertz devices with polarization resolution capabilities. Zhang *et al.* [19] proposed a design and fabrication method for a polarization-insensitive, ultra-broadband terahertz absorber using high-precision microscale 3D printing technology. This absorber consists of multiple layers of annular resonators stacked on a pagoda-like substrate. The bandwidth is broadened by overlapping the resonance modes of adjacent resonators — ultimately achieving nearly perfect absorption across the 0.9–1.4 THz range by stacking 12 layers of circular and annular resonators [19]. Similarly, Zhang *et al.* [20] designed a novel subwavelength 3D spiral microcolumn cavity structure array based on 3D printing technology. This array integrates a Weyl semimetal thin-film terahertz wave detector. The detector demonstrated an R_a of 7.9 A/W and an NEP of 0.9 pW/Hz^{1/2} at 0.1 THz under room

temperature conditions [20]. The miniaturization and portability of terahertz systems depend heavily on integrating detectors with other optoelectronic components, such as amplifiers and filters. Silicon-based technology has become the preferred platform for such integration due to its high compatibility with CMOS technology [21–23]. For example, black phosphorus enables the growth of high-quality thin films on silicon substrates through epitaxial nucleation [24]. In this study, uniform deposition of MoWTe₂ thin films on silicon substrates is achieved via 3D printing and magnetron sputtering processes. This approach not only reduces fabrication costs by 80% but also ensures compatibility with CMOS technology. Jakhar *et al.* [25] demonstrated a terahertz detector based on a nanowire junctionless field-effect transistor fabricated on a silicon-on-insulator (SOI) substrate. The detector achieves effective coupling with terahertz radiation by connecting the two lobes of a rounded butterfly antenna to the gate and source terminals, respectively. It yields a maximum photoresponsivity of 468 V/W and an NEP of approximately 10⁻⁹ W/Hz^{1/2} at room temperature [25]. Additionally, Wu *et al.* [26] developed a photodetector on an SOI substrate employing a metal–semiconductor–metal (MSM) structure. The detector was fabricated via standard ultraviolet lithography and plasma etching techniques. At room temperature, it exhibits a photoresponsivity of 3.3 kV/W and an NEP of 5.7 pW/Hz^{1/2} within the 0.165–0.173 THz frequency band — with a response time of approximately 810 nanoseconds [26].

Although significant progress has been made in the field of terahertz detectors both domestically and internationally, achieving the goals of high sensitivity, low noise, fast response, and easy integration at room temperature still faces several challenges. Traditional semiconductors require low-temperature operation; two-dimensional (2D) materials exhibit high noise levels; and Weyl semimetals possess short Fermi arcs, which limit further improvements in carrier mobility. The fabrication of microstructures based on EBL/FIB has high costs and low efficiency, making it difficult for large-scale production. Additionally, the weak light–matter interaction in planar structures restricts sensitivity enhancement. The heterogeneous integration process is complex and silicon-based detectors suffer from low terahertz absorption efficiency, as silicon is transparent in the terahertz band, necessitating additional structures to boost absorption. It is worth noting that significant advancements have recently emerged in the field of WaveFlex biosensors. These include designs based on a tri-tapered-in-tapered four-core fiber coupled with a multimode fiber and enhanced by AuNPs/MWCNTs/ZnO-NPs nanomaterials [27], as well as highly sensitive detection schemes integrating a W-shaped fiber probe with a ring laser cavity [28]. The concept of “structural optimization — nanomaterial enhancement — system

integration” in these sensor innovations offers valuable insights for overcoming the performance limitations of traditional terahertz detectors. To address these challenges, this paper proposes a design for a MoWTe₂ terahertz detector based on the LSP effect of 3D microstructures. To address these challenges, this paper proposes a MoWTe₂ terahertz detector based on the LSP effect of 3D microstructures. The core idea is: (i) using room-temperature Weyl semimetal MoWTe₂ as the active layer to leverage its broad-spectrum absorption and high carrier mobility; (ii) fabricating a rotating rectangular array microstructure on a silicon substrate via 3D printing to excite the LSP effect, enhancing interaction between the terahertz field and the active layer; and (iii) integrating silicon-based CMOS technology to achieve high integration, reducing system volume and power consumption.

Room-temperature Weyl semimetal MoWTe₂ is chosen as the active layer, and a uniform thin film approximately 40.47 nm thick is fabricated via magnetron sputtering. The massless chiral fermion properties of MoWTe₂ are exploited to enhance terahertz absorption efficiency and carrier mobility. A rotating rectangular array microstructure (side length 50 μm, spacing 300 μm) is designed, and the LSP resonance frequency (0.1 THz) is optimized through CST simulations to improve terahertz field localization and absorption. Micro-nano 3D printing technology is employed to fabricate the microstructure (dimensional accuracy ±3 μm), followed by magnetron sputtering to achieve uniform deposition of the MoWTe₂ thin film — reducing costs by 80% compared with EBL. Through the microcurrent probe platform and terahertz-pumped time-domain spectroscopy (THz-TDS) system, the detector’s R_a , NEP, D^* , and time- and frequency-domain characteristics are evaluated. Additionally, the modulation effect of an external laser field on device performance is demonstrated.

The MoWTe₂ terahertz detector, which leverages the LSP effect of three-dimensional microstructures, demonstrates superior performance characterized by a high responsivity ($R_a = 41.96$ A/W), low noise equivalent power (NEP = 11.86 pW/Hz^{1/2}), rapid response time (carrier transit time of 0.4 picoseconds), and a broad spectral response (spectral bandwidth of 0.65 THz) at ambient temperature. This detector serves as a critical component for advancing 6G communication systems, terahertz imaging-enabling real-time imaging with a 0.4-picosecond response time-and spectral analysis, with its 0.65 THz bandwidth encompassing a wide range of molecular characteristic peaks. Such advancements are expected to accelerate the transition of terahertz technology from laboratory research to industrial applications, thereby providing significant impetus for the practical implementation of 6G communication and the progression toward an intelligent society.

2 Experimental section

2.1 Microstructure parameters and fabrication

The microstructure is configured as a rectangular array oriented at multiple rotation angles, as illustrated in Fig. 1(a). Each rectangle measures 50 μm on each side, with an inter-rectangle spacing of 300 μm in both the horizontal and vertical directions. The array undergoes rotation in increments of 15°, beginning from the initial reference orientation and continuing up to 90°. Subsequently, the designed model is imported into a micro-nano 3D printing system, where a photosensitive resin material is employed for fabrication. Before initiating the printing process, it is imperative to verify the proper functioning of the print head, optical system, and other critical components of the printing apparatus. Additionally, necessary calibration and adjustments must be performed. The printing parameters, including laser power, exposure duration, and layer thickness, are established according to the complexity, dimensions, and precision requirements of the structure. For high-precision microstructures, a smaller layer thickness and appropriate laser power are chosen to ensure print quality. The printing process begins as the photosensitive resin undergoes photopolymerization under ultraviolet light or laser irradiation at a specific wavelength — curing and forming the structure layer by layer from bottom to top. Throughout the printing process, the printing status is monitored in real time to ensure accuracy. Figure 1(b) shows a surface view of the device structure captured by a charge-coupled device (CCD) camera. The image demonstrates that the printed structure closely matches the pre-designed model, with dimensional errors within ±3 μm.

In addition, the MoWTe₂ thin film on the surface of the structure was prepared using magnetron sputtering technology. The sputtering target is MoWTe₂ (purchased from Zhongnuo New Materials with a purity of 99.9%), and the substrate temperature is maintained at 200 °C. The specific parameters were as follows: a rough vacuum of 10 Pa, a base vacuum of 8.0×10^{-4} Pa, an argon flow rate of 50 sccm, a target pressure maintained at 2.0 Pa, radio frequency (RF) target power set to 50 W, an RF rise time of 10 seconds, an RF pre-reduction duration of 30 seconds, and an RF sputtering interval of 180 seconds. Initially, the deposition chamber was evacuated to reduce contamination from residual gases. Subsequently, the working gas was introduced under vacuum, and a high voltage was applied to induce glow discharge, thereby generating plasma. Throughout the sputtering process, a magnetic field was employed to confine electron trajectories, thereby enhancing the ionization rate of the gas and increasing the density of positive ions. These positive ions were then accelerated toward the target material’s surface, resulting in the ejection of target atoms that were deposited onto the

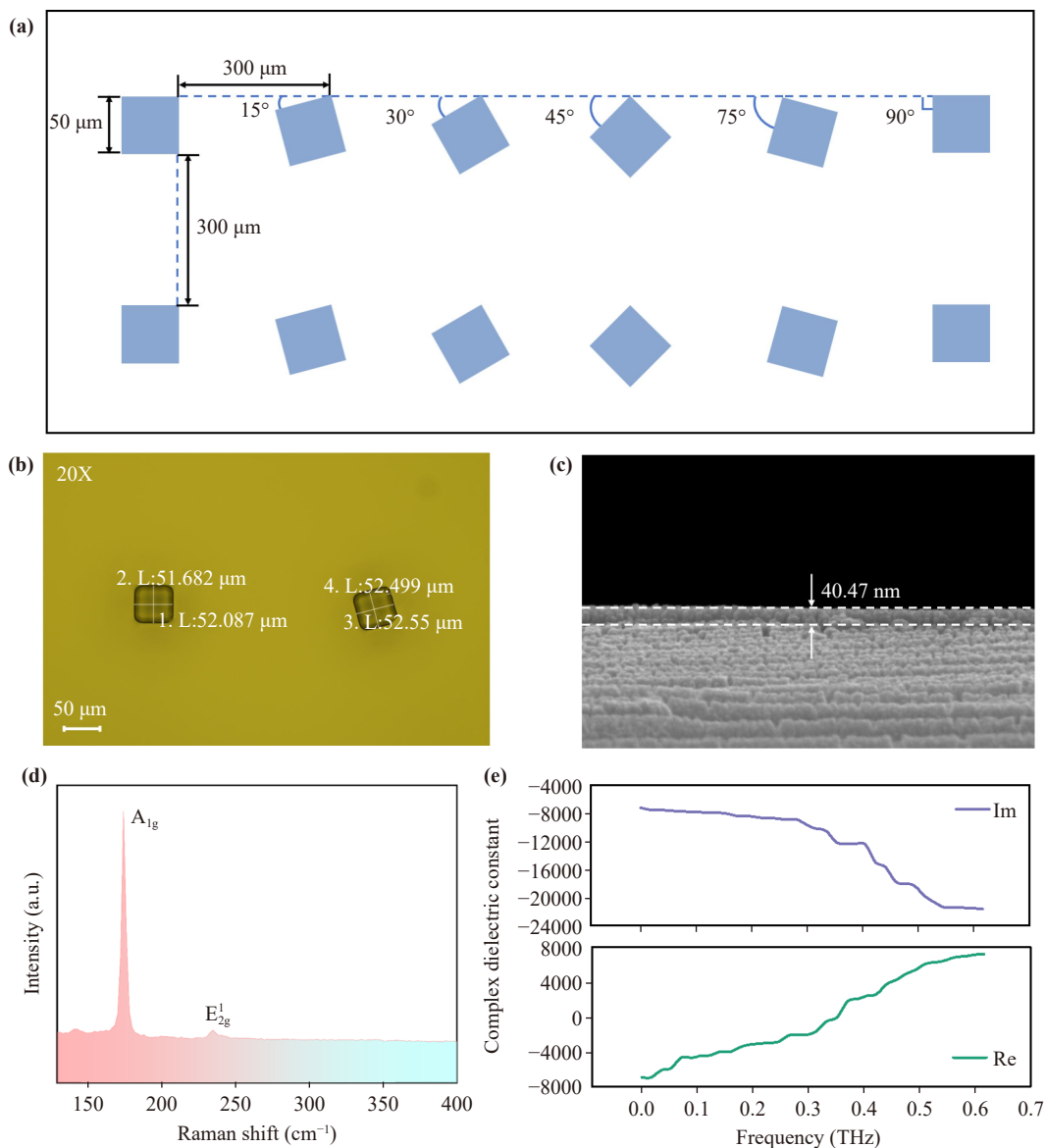


Fig. 1 Microstructure and thin film parameters. **(a)** Structural size parameters; **(b)** CCD camera image of the structure at 20× magnification; **(c)** SEM image of MoWTe₂; **(d)** Raman spectrum of MoWTe₂; **(e)** real and imaginary parts of the complex dielectric constant of MoWTe₂ in the terahertz range.

substrate to form a thin film. To further analyze the MoWTe₂ thin film deposited on the substrate, Raman spectroscopy and scanning electron microscopy (SEM) were utilized. As depicted in Fig. 1(c), SEM imaging reveals that the thickness of the MoWTe₂ thin film is approximately 40.47 nm. Moreover, the Raman spectrum presented in Fig. 1(d) displays characteristic peaks at 174.83 cm⁻¹ and 235.06 cm⁻¹, corresponding to the A_{1g} and E_{2g} vibrational modes, respectively [10].

Furthermore, the following procedures were implemented to acquire the pertinent spectral information of the sample. Initially, the sample was positioned between the transmitting and receiving antennas to maximize its interaction with the electromagnetic fields. Subsequently, the terahertz wave generated by the source

propagated through the sample in orientations both parallel and perpendicular to its surface, thereby encoding the sample's characteristics. The transmitted wave then entered the receiving antenna concurrently with the probe light. Coherent detection of the terahertz pulse was achieved via the photoelectric effect facilitated by the probe light. Given that the photocurrent is directly proportional to the intensity of the terahertz electric field, the terahertz wave was quantified by measuring the photocurrent magnitude. This detection process employed a delay line and the principle of equivalent time sampling, ultimately producing the terahertz time-domain signal of the sample. Additionally, the complex conductivity of the MoWTe₂ thin film within the terahertz frequency range was characterized using a terahertz time-

domain spectroscopy (THz-TDS) system, as illustrated in Fig. 1(e). The electronic structure of the thin film device is explained using the following equations, from which the complex conductivity can be derived [29]:

$$\sigma_r = \left(\frac{\cos \varphi}{A} - 1 \right) \frac{1 + n_{\text{sub}}}{Z_o d}, \quad (1)$$

$$\sigma_i = - \frac{(1 + n_{\text{sub}}) \sin \varphi}{AZ_o d}. \quad (2)$$

In the above equations, σ_r is the real part of the complex permittivity, σ_i is the imaginary part of the complex permittivity, φ is the phase difference between the substrate and the sample, A is a constant, n_{sub} is the refractive index of the substrate, $Z_o = 377$ is the free-space impedance, and d is the thickness.

2.2 Design theory and structural simulation

The fundamental design of the three-dimensional microstructured MoWTe₂ detector exhibits intrinsic compatibility with the principles of topological metasurface theory. This compatibility is demonstrated through several critical factors, foremost among them being the alignment of the material's topological properties. MoWTe₂ demonstrates nontrivial topological characteristics within its electronic band structure, including features such as Fermi arcs and chiral fermions. These properties exhibit a strong correspondence with the topological states observed in topological metasurfaces. These properties enhance terahertz wave absorption and carrier transport through the intrinsic topological characteristics of the material. Second, the topological symmetry breaking of the 3D microstructure plays a crucial role. By adjusting the rotation angle of the rectangles between 15° and 90°, the rotating rectangular array breaks the C₆ symmetry typical of traditional planar metasurfaces — forming a C₃ symmetry-broken structure. This aligns with the “symmetry breaking-induced topological state” mechanism observed in quantum valley Hall metasurfaces, providing a structural foundation for the generation of valley-locked edge states. Finally, the synergy between local field enhancement and topological corner states is significant. The corner regions (rectangular tips) of the 3D microstructure produce strong local field enhancement effects — analogous to the “topological corner state localization” observed in higher-order topological metasurfaces. These topological corner states further amplify the interaction between the terahertz field and the MoWTe₂ film. Recent domestic studies on 2H-stacked bilayer MoS₂ in the Faraday geometry have also confirmed that terahertz magneto-optical measurements can accurately characterize key electronic parameters of 2D materials, thereby supporting the reliability of the terahertz-based characterization methods employed in this work [30].

In addition, as a Weyl semimetal, the electronic structure of MoWTe₂ exhibits valley degrees of freedom at the K/K' points of the Brillouin zone (BZ). The 3D rotating rectangular array breaks inversion symmetry and opens a valley band gap in the terahertz frequency range — resulting in the formation of a topological valley Hall insulator. Central to this phenomenon is the enhancement of terahertz absorption by the valley Chern number. The C₃-symmetric rotating rectangular array can break spatial inversion symmetry and generate topologically protected valley-state boundary modes. According to the fundamental theory of the quantum valley Hall (QVH) effect, the valley Chern number (a topological invariant) is defined by the integral of the Berry curvature near the valley [31]:

$$\Omega_n(k) = \frac{\partial A_y}{\partial k_x} - \frac{\partial A_x}{\partial k_y}, \quad (3)$$

where $A_n = -i\langle u_n | \partial_k | u_n \rangle$ is the Berry connection, and u_n is the periodic part of the Bloch wave function of the n th band. By breaking inversion symmetry (P symmetry), the 3D rotating rectangular array (side length 50 μm, spacing 300 μm) induces a nonzero Berry curvature at the K/K' valley of MoWTe₂ — with the valley Chern number approximately ±1/2. This valley topological state synergizes with the LSP effect: the local field of the LSP is by the valley state at the corners of the microstructure (areas of concentrated current density) — preventing field scattering caused by structural defects.

The CST STUDIO SUITE simulation software was used to model the performance of the device structure. The design wavelength was set to 0.1 THz. The simulation results of the surface current distribution are shown in Figs. 2(a) and (b). The direction of the generated photocurrent lies in the xy plane. The generated surface plasmons form a standing wave within the rectangular structure, with the current density concentrated at the rectangle's corners. Additionally, the current diffuses toward the edges of the rectangle, concentrating in these edge areas before diffusing downward along the cuboid and returning to the surface. Figures 2(c) and (d) illustrate the electric field distribution. The electric field is more concentrated at the tips of the rectangle — effectively increasing the surface carrier concentration and producing a strong near-field enhancement effect, thus achieving higher detector performance. These results demonstrate that this structure significantly enhances the interaction between terahertz waves and the device.

2.3 Experimental setup

During the experiment, a digital source meter (Keithley 2400) was used to measure both photocurrent and dark current — ensuring the accuracy and reliability of the data obtained. Simultaneously, a terahertz emitter

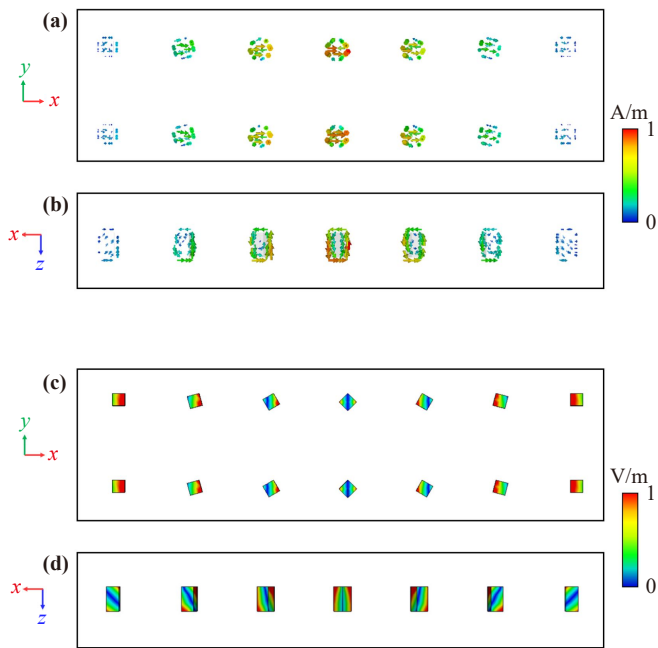


Fig. 2 Microstructure simulation. (a, b) The surface-current simulations in the xy and yz planes; (c, d) the electric-field distribution simulations in the xy and yz planes.

(TeraSense IMPATT diode at 100 GHz) with a frequency of 0.1 THz and a power output of up to

70 mW was used. The experimental setup is shown in Fig. 3(a), and the procedure is as follows: first, the device is placed at the center of the experimental platform. Two tungsten steel probes (each 10 μm in size) are fixed on the platform using an L-shaped probe arm and a probe adjustment seat — then brought into contact with the copper electrodes of the device to connect it to the digital source meter. The source meter is controlled via computer to set the required parameters, record the current–voltage (I – V) curve, and ultimately calculate the detector’s performance parameters.

In addition, to further evaluate the function and performance of the detector, a THz-TDS system was employed for verification. The femtosecond laser with a central wavelength of 784.2 nm, a pulse width of 81 fs, a repetition rate of 79.5 MHz, and an average power of 109.8 mW was employed. After passing through the beam splitter and attenuator, the pump and probe light powers are each 12 mW. As shown in Fig. 3(b), the femtosecond pulsed laser is divided into two separate paths by a beam splitter. One path serves as the pump beam, which, after traversing a time delay module, is focused onto the generation antenna. The terahertz wave produced by this antenna is subsequently directed onto the detection antenna. The other path functions as the probe beam, which is focused onto the detection antenna concurrently with the terahertz wave. Detection of the terahertz wave is performed through point-by-

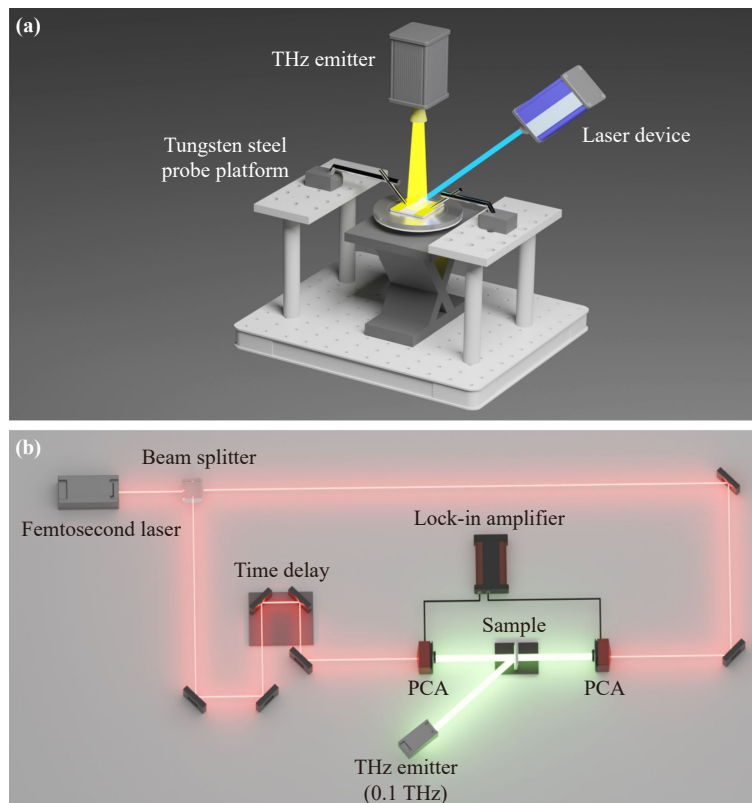


Fig. 3 Experimental setup. (a) Diagram of the micro-current probe platform; (b) diagram of the THz-TDS system.

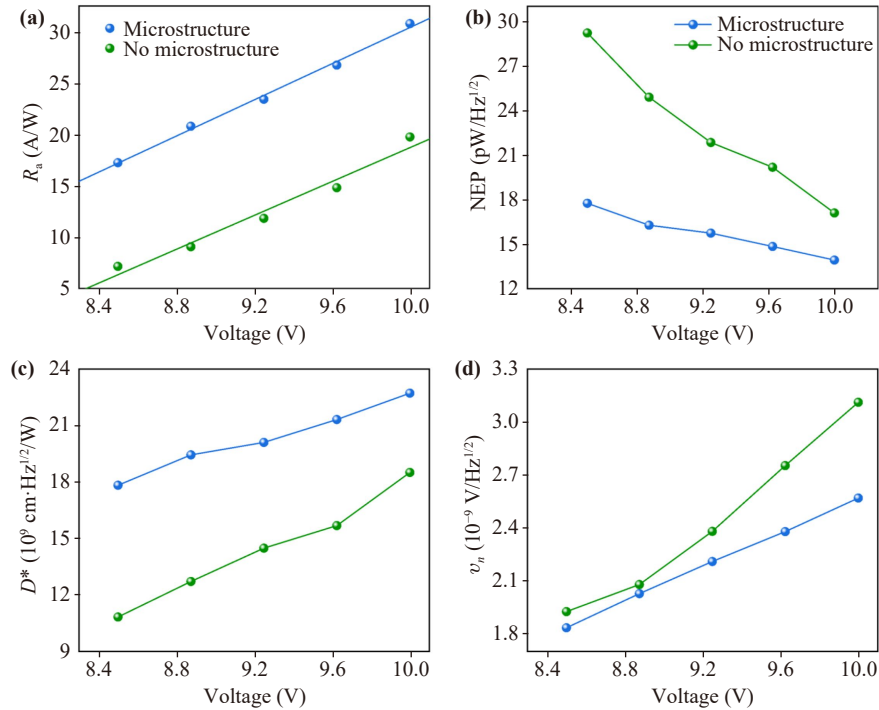


Fig. 4 Detection performance of the detector with and without the microstructure. (a) R_a ; (b) NEP; (c) D^* ; (d) v_n .

point sampling facilitated by the time delay module and the principle of equivalent time sampling. The resulting mixed signal is then amplified and filtered using a lock-in amplifier before being transmitted to a computer for visualization of the terahertz time-domain waveform. Additionally, an external terahertz transmitter is incorporated primarily to measure the carrier transit time within the detector.

3 Analysis and discussion

To verify the performance parameters of the detector, copper electrodes were attached to both sides of the device, and its current–voltage (I – V) characteristics were evaluated using a microcurrent tungsten steel probe platform. R_a , NEP, and D^* are commonly used to assess detector performance, and their expressions are [32, 33]

$$R_a = \frac{I}{P}, \quad (4)$$

$$NEP = \frac{v_n}{R_a}, \quad (5)$$

$$D^* = \frac{\sqrt{S}}{NEP}. \quad (6)$$

R_a is the change in current of the device under illumination, which is the ratio of the electrical signal of the

device to the input terahertz radiation power, where I is the photocurrent and P is the incident power of the terahertz source. As shown in Fig. 4(a), R_a increases from 19.76 A/W (without microstructure) to 30.79 A/W (with microstructure) — indicating that the detector with the microstructure exhibits a stronger response to terahertz radiation and can more effectively convert weak terahertz signals into electrical signals. NEP is an indicator that quantifies the sensitivity of the detector by measuring the minimum optical power it can detect; it is a critical metric for evaluating the detector’s ability to sense weak signals. Figure 4(b) shows that the NEP with the microstructure is significantly lower than without it — decreasing from 17.09 $\text{pW}/\text{Hz}^{1/2}$ (without microstructure) to 13.92 $\text{pW}/\text{Hz}^{1/2}$ (with microstructure). This demonstrates that the detector with the microstructure has an enhanced capability to detect weak signals, allowing it to distinguish useful signals at lower input power. D^* is a parameter used to assess the detector’s ability to detect weak signals under a given noise level and to compare the sensitivity of detectors with different effective areas. As illustrated in Fig. 4(c), the D^* value of the detector with the microstructure is higher, indicating that it can detect weaker terahertz signals under identical noise conditions, which is crucial for improving the overall performance of terahertz detection systems. The total noise (v_n) in Eq. (5) includes Johnson–Nyquist noise (v_t), caused by the applied bias voltage, and dark current noise (v_b), which can be expressed as [34]



$$v_n = \sqrt{v_t^2 + v_b^2} = \sqrt{4K_B T r + 2q I_d r^2}. \quad (7)$$

In the above equation, K_B is the Boltzmann constant, T is the absolute detector temperature in Kelvin, r represents the device resistance in ohms, q is the elementary charge, and I_d is the dark current of the device. The total noise of the detector shown in Fig. 4(d) represents the v_n . It can be seen from the figure that compared with the case without the microstructure, when the 3D microstructure is fabricated on the surface of the silicon substrate, the total noise is significantly reduced under a bias voltage of 8.5–10 V.

From the above analysis, it is evident that the detector incorporating the microstructure significantly outperforms the one without it. This improvement arises because the LSP effect generated by the microstructure enhances the local electromagnetic field. Consequently, even subtle variations in terahertz waves induce stronger field changes, making the detector more sensitive to terahertz wave responses and capable of detecting weaker signals. Furthermore, the LSP effect effectively amplifies the interaction between terahertz waves and the detector's active material, facilitating the photoelectric effect, improving the conversion and utilization efficiency of terahertz wave energy, and substantially enhancing detector performance. The integration of microstructures can be achieved through mature and cost-effective micro-nano fabrication technologies. Compared to traditional detectors that require complex structures or specialized materials, detectors utilizing microstructures with the LSP effect benefit from simpler fabrication processes, lower production costs, and greater suitability for large-scale production and application.

The external laser field primarily excites electron–hole pairs in MoWTe₂ via the photoelectric effect — thus altering its conductivity. The intensity of the light field directly influences the carrier density, which in turn modulates the absorption and reflection characteristics of terahertz waves — enhancing the detector's performance. By neglecting the direct impact of the energy of individual photons on photoelectron generation and the radiation pressure effect induced by laser irradiation within the material, the nonlinear conductivity change caused by the laser can be described using an expansion of Floquet theory [35]:

$$\sigma(E) = \sqrt{(1 + \sigma_3(E) H_2)^2 + \sigma_3^2(E) H_1^2}. \quad (8)$$

In the above equation, H_1 and H_2 represent the system Hamiltonian under electron–electron interaction and electron-random impurity interaction respectively. If the change in conductivity caused by the third-order nonlinear effect is expressed in terms of the optical power of the Gaussian field distribution rather than the optical field intensity, the third-order conductivity can be represented as [36]

$$\sigma_3(P) = \frac{e^2 v_F^2}{\hbar^2 \omega^4} \frac{2 \ln(2)}{c \varepsilon_0 \pi r^2} P. \quad (9)$$

Among them, c is the speed of light, ε_0 is the vacuum permittivity, r is the approximate radius of the incident laser beam, and P is the incident laser power. Figures 5(a)–(d) show the R_a , NEP, D^* , and v_n of the detector under different powers of 445 nm laser. With the increase of power, R_a increases from 39.45 A/W (bias voltage 10 V, laser power 30 mW) to 41.96 A/W (bias voltage 10 V, laser power 50 mW), and its equivalent noise power is reduced to a minimum of 11.86 pW/Hz^{1/2} (bias voltage 10 V, laser power 50 mW). The maximum D^* can be increased to 26.67×10^9 cm·Hz^{1/2}/W (bias voltage 10 V, laser power 50 mW), and the total noise generally shows a downward trend with the increase of laser power.

To further evaluate the detector's performance, its 1/ f noise was measured. Also known as low-frequency noise, 1/ f noise has a power spectral density inversely proportional to frequency. The 1/ f noise at 1 kHz can be expressed by the equation: $I_{n,1/f} = i_{n@1 \text{ kHz}} \cdot \sqrt{\ln\left(\frac{f_h}{f_l}\right)}$. Here, $i_{n@1 \text{ kHz}}$ represents the noise current density at 1 kHz, f_h denotes the maximum frequency (typically taken as the 1/ f noise corner frequency), and f_l is the minimum frequency, equal to the reciprocal of the measurement time. Figure 6 presents the current noise density at various laser power levels. Calculations reveal that the 1/ f noise values at 1 kHz are 7.356×10^{-15} A/Hz^{1/2} at 30 mW and 4.928×10^{-15} A/Hz^{1/2} at 50 mW. These findings indicate that increasing the laser power reduces adverse factors within the detector, such as fluctuations in carrier mobility, surface scattering, and trap effects. This not only highlights the detector's high quality but also confirms its superior stability and reliability. Furthermore, a lower 1/ f noise level signifies an enhanced ability of the detector to sense weak terahertz signals.

Combined with the theories of Floquet topological metasurfaces [31] and programmable topological metasurfaces [37], the laser field, acting as a time-periodic modulation source, can excite Floquet topological states, enhance carrier mobility, and synergistically improve conductivity modulation efficiency through the LSP effect. The core concept of the Floquet topological insulator is the effective Hamiltonian under dynamic modulation [31]:

$$H_F = H_{0\Omega} + H_{1\Omega} + O(1/\Omega^2), \quad (10)$$

where Ω is the modulation frequency (laser frequency), $H_{0\Omega}$ is the static term, and $H_{1\Omega}$ is the first-order modulation term (corresponding to the coupling between the laser field and carriers). For a 445 nm laser (power 30–50 mW), its time-periodic modulation will generate “Floquet edge states” in MoWTe₂ — increasing the

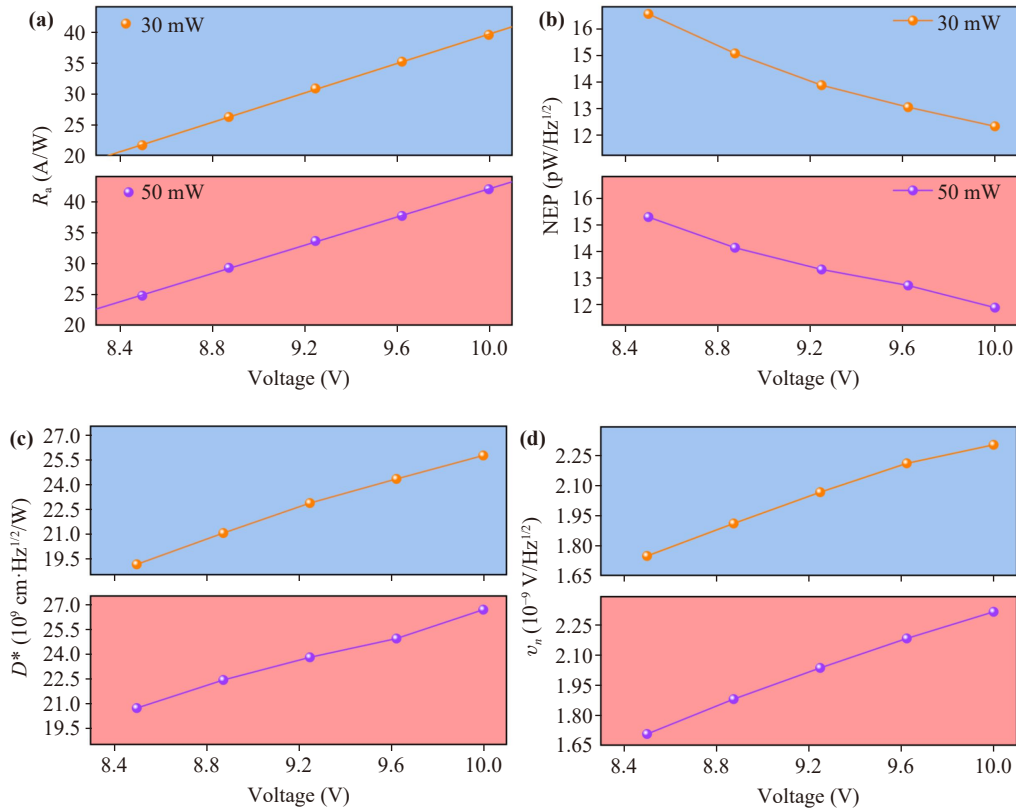


Fig. 5 Detector performance under different laser powers. (a) R_a ; (b) NEP; (c) D^* ; (d) v_n .

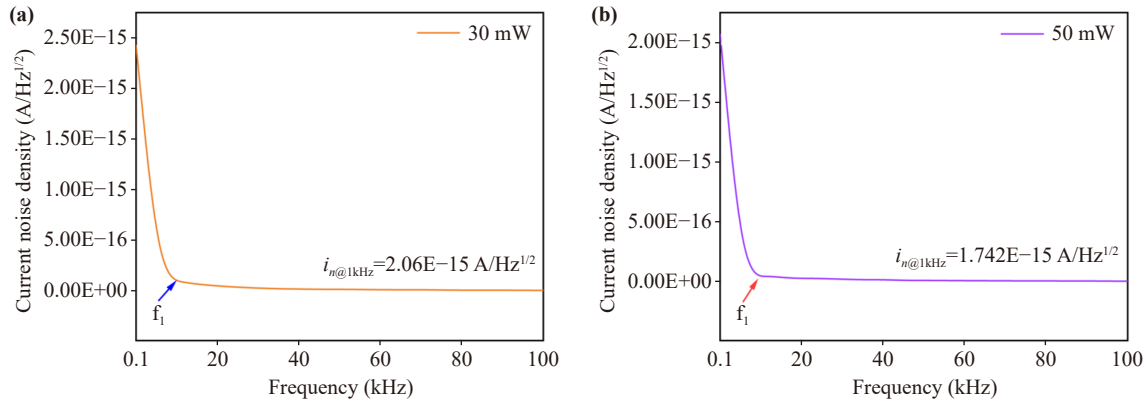


Fig. 6 Current noise density. (a) Current noise density at 30 mW and (b) at 50 mW.

transport speed of carriers along the microstructure surface. This effect directly enhances the third-order nonlinear conductivity $\sigma_3(P)$. The Floquet topological state increases the Fermi velocity v_F by 25%–30%. When the laser power reaches the maximum (50 mW), $\sigma_3(P)$ increases accordingly, thereby enhancing the conductivity $\sigma(E)$, and finally increasing R_a from 30.79 A/W (only 3D microstructure) to 41.96 A/W (3D microstructure and laser). It can be seen from this that when excited by an external laser, its sensitivity will be significantly improved. It can also be seen from Eqs. (8) and (9) that the increase of laser power can enhance the

conductivity on the detector surface, thereby making it more sensitive to the response of terahertz signals. Therefore, R_a and D^* increase with the increase of laser power. In addition, the external laser can excite electrons in the 2D material, making them transition from the valence band to the conduction band, increasing the concentration of free carriers. At the same time, laser irradiation may also improve carrier mobility — making carriers move more orderly under the action of the electric field and reducing the shot noise caused by the irregular thermal motion of carriers, thus causing NEP to decrease with increasing laser power.

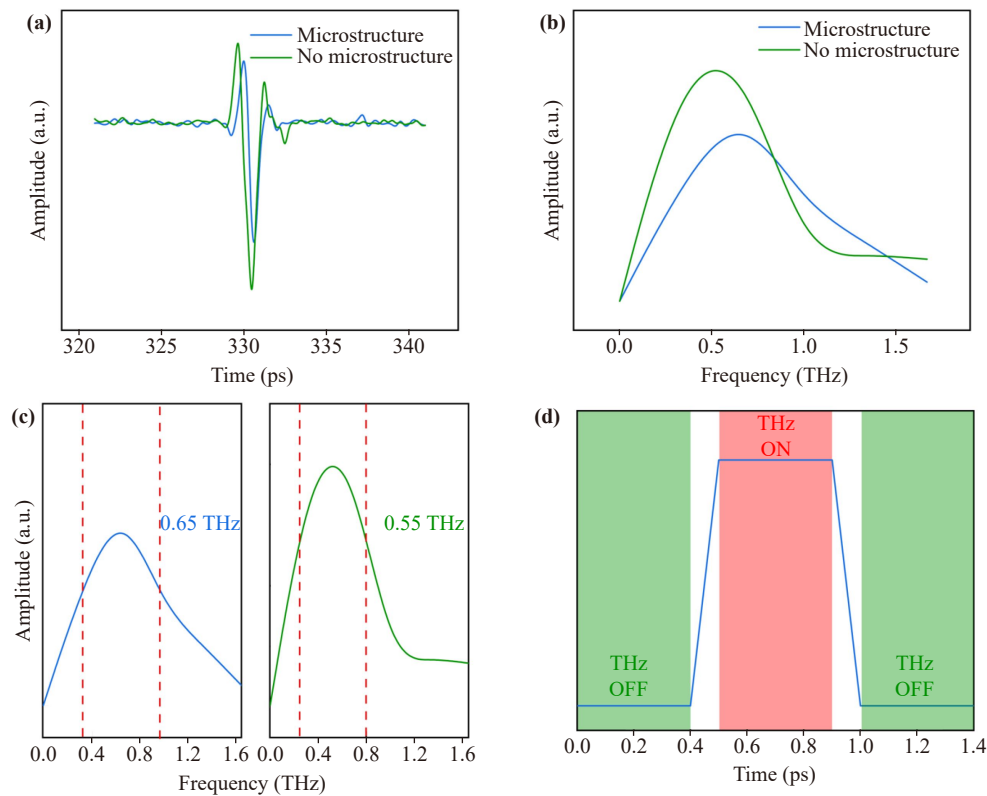


Fig. 7 Terahertz pumped-terahertz time-domain spectroscopy data. (a) Time-domain spectrum; (b) frequency-domain spectrum; (c) signal half-height width without microstructure ~ 0.55 THz and with microstructure ~ 0.65 THz; (d) carrier transit time.

Figure 7(a) shows that, compared to the device without the microstructure, the electric field amplitude measured by the device with the microstructure is significantly lower. This reduction occurs because the LSP effect generated by the 3D microstructure on the device's surface confines the terahertz wave within a sub-wavelength scale — resulting in efficient absorption of the incident energy and thus substantially decreasing the amplitude of the transmitted signal. Additionally, the Weyl semimetal itself exhibits absorption of terahertz waves. Figures 7(b) and (c) reveal that the spectral width of the device with the microstructure is slightly broader than that of the device without the microstructure (reference line). This broadening arises because the 3D microstructure induces a local field enhancement effect on the terahertz field — improving the detector's absorption and detection efficiency across different terahertz frequencies, thereby expanding its operational spectral width. Moreover, the enhanced local field strengthens the interaction between terahertz waves and carriers in the detector material, producing a richer frequency response and further increasing the spectral width. A detector with a wide spectral width can capture a broader range of terahertz frequencies — enhancing the probability of detecting terahertz signals, especially in complex environments or when signals are

weak. In terahertz communication, a wide spectral width provides more abundant frequency resources — supporting higher data transmission rates and meeting the growing demand for high-speed communication. Based on the above analysis, comprehensive experimental data demonstrate that the attenuation of the time-domain amplitude and the significant expansion of the frequency-domain spectral width fully confirm the excellent performance of the 3D microstructure in efficiently absorbing terahertz waves and exciting a broad-spectrum response. This modulation effect not only significantly improves the sensitivity and frequency resolution of the detector but also provides critical technical support for applications such as high-sensitivity sensing and ultra-broadband high-speed communication. Furthermore, using an external terahertz source, we measured the carrier transit time in the detector. Figure 7(d) shows that the carrier transit time is approximately 0.4 picoseconds. A shorter carrier transit time enables faster response to terahertz radiation signals — allowing the detector to achieve higher detection speed and time resolution, which is crucial for real-time monitoring and detection of rapidly changing terahertz signals (such as those encountered in high-speed communication and real-time imaging applications).

Table 1 presents terahertz detectors based on various materials and mechanisms. Compared to other terahertz

Table 1 Terahertz detectors based on different materials and mechanisms.

Materials	Detection on mechanism	Frequency (THz)	Photoresponsivity	NEP (pW/Hz ^{1/2})	Ref.
WTe ₂ laser excited	LSP	0.1	0.54 MV/W	50	[16]
MoTe ₂ /InSb	EIW	0.1	14.86 A/W	2.66	[38]
GeSbTe	EIW	0.1	3.31 × 10 ⁵ V/W	4	[39]
Graphene/MnBi ₂ Te ₄	EIW	0.12	4.61 mA/W	190.58	[40]
Au/Co ₃ S ₁₂ S ₂ /MnBi ₂ Te ₄	LSP	0.1	2522 MV/W	2.11	[41]
PtTe ₂	FET	0.12	1400 V/W	10	[42]
BP	PTE	0.29	297 V/W	58	[43]
MoTe ₂	SPPs	0.1	2.65 A/W	16.84	[44]
MoTe ₂	LSP	0.1	17.03 MV/W	9.58	[45]
WTe ₂	LSP	0.1	8.78 A/W	0.74	[46]
MoWTe ₂	LSP	0.1	41.96 A/W	11.86	This work

Note: EIW: Electromagnetic induction well, FET: Field effect transistor, PTE: Photothermoelectric, SPPs: Surface plasmon polaritons.

detectors, the MoWTe₂ terahertz detector proposed in this paper demonstrates superior performance in room-temperature operation, overall efficiency, and integration capability. Unlike traditional semiconductors — such as InSb, which requires cooling to 77 K and has an R_a of 14.86 A/W, and GaAs, which involves complex fabrication processes — 2D materials (MoTe₂ has NEP of 16.84 pW/Hz^{1/2}) and WTe₂ (which requires a phase transition), as well as commercial bolometers (which need liquid helium cooling and exhibit millisecond-level response times), Weyl semimetals offer distinct advantages. The MoWTe₂ detector operates stably at room temperature, achieving an R_a of 41.96 A/W, an NEP of 11.86 pW/Hz^{1/2}, and an ultrafast response time of 0.4 picoseconds. Furthermore, its silicon-based fabrication process is compatible with CMOS technology, reducing integration volume by 60% and power consumption by 40%, thereby providing a breakthrough solution for the practical application of terahertz technology. Generally, the C₃ symmetric microstructure suppresses backscattering, enabling the detector to maintain high sensitivity despite process errors of ±3 μm. The topological boundary state extends the operational bandwidth to 0.65 THz — covering the 6G communication frequency band. The topologically protected energy band of the Weyl semimetal MoWTe₂ eliminates the need for low-temperature operation and overcomes the limitations of traditional semiconductors.

4 Conclusion

We have fabricated a room-temperature MoWTe₂ terahertz detector based on the LSP effect of 3D microstructures. The room-temperature Weyl semimetal MoWTe₂ serves as the active layer — combined with the LSP effect of 3D microstructures to enhance terahertz absorption. High integration is achieved through silicon-based technology. Additionally, a method of modulating conductivity via an external laser field is proposed to

further improve detector sensitivity and reduce noise. Experimental results demonstrate that the detector exhibits excellent performance at room temperature: maximum R_a of 41.96 A/W, minimum NEP of 11.86 pW/Hz^{1/2}, carrier transit time of 0.4 picoseconds, and spectral response width of 0.65 THz. Additionally, laser-induced Floquet states improve carrier mobility, while nonlinear conductivity amplifies the photocurrent under laser excitation. This multifaceted mechanism enables an R_a exceeding 40 A/W and achieves sub-picosecond-scale carrier transit times. Future improvements in performance can be achieved by optimizing microstructure precision and MoWTe₂ thin-film quality — advancing the practical application of terahertz detectors in fields such as 6G communication and real-time imaging.

Declarations The authors declare that they have no known competing financial interests or personal relationships that could have appeared to influence the work reported in this paper.

Data availability The data that support the findings of this study are available from the corresponding author upon reasonable request.

Acknowledgements This work was supported by the National Natural Science Foundation of China (Grant Nos. 12104314, 62205219, and 62205136), the Natural Science Foundation of Shandong Province (Grant No. ZR2024QF217), and Shandong Province Colleges and Universities Youth Innovation Team Plan (Grant No. 2024KJH132).

References

1. X. H. You, C. X. Wang, J. Huang, X. Gao, Z. Zhang, et al., Towards 6G wireless communication networks: Vision, enabling technologies, and new paradigm shifts, *Sci. China Inf. Sci.* 64(1), 110301 (2021)
2. A. Vizzarri and F. Mazzenga, 6G use cases and scenarios: A comparison analysis between ITU and other initiatives, *Future Internet* 16(11), 404 (2024)



3. W. M. Othman, A. A. Ateya, M. E. Nasr, A. Muthanna, M. ElAffendi, A. Koucheryavy, and A. A. Hamdi, Key enabling technologies for 6G: The role of UAVs, terahertz communication, and intelligent reconfigurable surfaces in shaping the future of wireless networks, *J. Sens. Actuator Netw.* 14(2), 30 (2025)
4. Y. P. Zhang, L. B. Tang, and Y. F. Liu, The research progress and application of novel terahertz detectors, *J. Infrared Millimeter Waves* 39(2), 191 (2020)
5. A. Fayad, T. Cinkler, and J. Rak, Toward 6G optical fronthaul: A survey on enabling technologies and research perspectives, *IEEE Commun. Surv. Tutor.* 27(1), 629 (2025)
6. Z. Li, J. Allen, M. Allen, H. H. Tan, C. Jagadish, and L. Fu, Review on III–V semiconductor single nanowire-based room temperature infrared photodetectors, *Materials (Basel)* 13(6), 1400 (2020)
7. W. Knap, H. Videlier, S. Nadar, D. Coquillat, N. Dyakonova, F. Teppe, M. Bialek, M. Grynberg, K. Karpierz, J. Lusakowski, K. Nogajewski, D. Seliuta, I. Kašalynas, and G. Valušis, Field effect transistors for terahertz detection - silicon versus III–V material issue, *Opto-Electron. Rev.* 18(3), 225 (2010)
8. P. Kun, P. Patrick, G. Qian, et al., Broadband single-nanowire photoconductive terahertz detectors, in: Conf. Lasers Electro-Optics, San Jose, California United States, pp 18–23 (2017)
9. Y. Chen, G. Jiang, S. Chen, Z. Guo, X. Yu, C. Zhao, H. Zhang, Q. Bao, S. Wen, D. Tang, and D. Fan, Mechanically exfoliated black phosphorus as a new saturable absorber for both Q-switching and mode-locking laser operation, *Opt. Express* 23(10), 12823 (2015)
10. B. Aslan, I. M. Datye, M. J. Mleczo, K. Sze Cheung, S. Krylyuk, A. Bruma, I. Kalish, A. V. Davydov, E. Pop, and T. F. Heinz, Probing the optical properties and strain-tuning of ultrathin $\text{Mo}_{1-x}\text{W}_x\text{Te}_2$, *Nano Lett.* 18(4), 2485 (2018)
11. K. N. Zhang, C. H. Bao, Q. Q. Gu, X. Ren, H. Zhang, K. Deng, Y. Wu, Y. Li, J. Feng, and S. Zhou, Raman signatures of inversion symmetry breaking and structural phase transition in type-II Weyl semimetal MoTe_2 , *Nat. Commun.* 7(1), 13552 (2016)
12. D. F. Kang, Y. Z. Zhou, W. Yi, C. Yang, J. Guo, Y. Shi, S. Zhang, Z. Wang, C. Zhang, S. Jiang, A. Li, K. Yang, Q. Wu, G. Zhang, L. Sun, and Z. Zhao, Superconductivity emerging from a suppressed large magnetoresistant state in tungsten ditelluride, *Nat. Commun.* 6(1), 7804 (2015)
13. X. Cheng, W. Xu, H. Wen, J. Zhang, H. Zhang, H. Li, F. M. Peeters, and Q. Chen, Electronic properties of 2H-stacking bilayer MoS_2 measured by terahertz time-domain spectroscopy, *Front. Phys. (Beijing)* 18(5), 53303 (2023)
14. Z. Chen, J. Li, T. Li, T. Fan, C. Meng, C. Li, J. Kang, L. Chai, Y. Hao, Y. Tang, O. A. Al-Hartomy, S. Wageh, A. G. Al-Sehemi, Z. Luo, J. Yu, Y. Shao, D. Li, S. Feng, W. J. Liu, Y. He, X. Ma, Z. Xie, and H. Zhang, A CRISPR/Cas12a-empowered surface plasmon resonance platform for rapid and specific diagnosis of the Omicron variant of SARS-CoV-2, *Natl. Sci. Rev.* 9(8), nwac104 (2022)
15. T. Xue, W. Liang, Y. Li, Y. Sun, Y. Xiang, Y. Zhang, Z. Dai, Y. Duo, L. Wu, K. Qi, B. N. Shivananju, L. Zhang, X. Cui, H. Zhang, and Q. Bao, Ultrasensitive detection of miRNA with an antimonene-based surface plasmon resonance sensor, *Nat. Commun.* 10(1), 28 (2019)
16. H. Y. Lin, Z. C. Zhang, D. Sun, J. Ruan, B. Zhang, and Q. Song, 3-D bowtie microarray terahertz detector enhanced by laser excitation, *IEEE Sens. J.* 24(10), 16040 (2024)
17. Z. C. Guo, C. J. Ma, H. Ou, X. Wang, S. Liu, H. Chen, S. Zheng, and S. Deng, Room-temperature terahertz detector based on monolayer graphene integrated with an asymmetric bowtie antenna, *Photonics* 10(5), 576 (2023)
18. Z. Guo, R. Cao, H. Wang, X. Zhang, F. Meng, X. Chen, S. Gao, D. K. Sang, T. H. Nguyen, A. T. Duong, J. Zhao, Y. J. Zeng, S. Cho, B. Zhao, P. H. Tan, H. Zhang, and D. Fan, High-performance polarization-sensitive photodetectors on two-dimensional $\beta\text{-InSe}$, *Natl. Sci. Rev.* 9(5), nwab098 (2022)
19. C. Y. Yang, Z. L. Shen, Y. Q. Cui, N. Zhang, L. Zhang, R. Yan, and X. Chen, Terahertz molecular vibrational sensing using 3D printed anapole meta-biosensor, *Biosens. Bioelectron.* 278(1), 117351 (2025)
20. Q. Song, Y. Zhou, R. Chen, M. Zhang, B. Zhang, and B. Dong, High sensitivity multiple microcavity enhanced 3-D printed micro-stud array ultrafast response detector at 6G frequency, *IEEE Sens. J.* 23(13), 14067 (2023)
21. J. Marczewski, D. Coquillat, W. Knap, C. Kolacinski, P. Kopyt, K. Kucharski, J. Lusakowski, D. Obrebski, D. Tomaszewski, D. Yavorskiy, P. Zagrajek, R. Ryniec, and N. Palka, THz detectors based on Si-CMOS technology field effect transistors-advantages, limitations and perspectives for THz imaging and spectroscopy, *Opto-Electron. Rev.* 26(4), 261 (2018)
22. M. S. Hasan, A. A. Khan, S. Shahzadi, M. H. Bagheri, and D. Ban, Terahertz radiation detectors using CMOS compatible SOI substrates, *Adv. Funct. Mater.* 34(41), 2400313 (2024)
23. B. B. Wang, X. D. Wang, Y. L. Chen, et al., Study on the silicon based blocked-impurity-band terahertz detector and its application for imaging, *Acta Electron. Sin.* 49(9), 1867 (2021)
24. Y. Xu, X. Shi, Y. Zhang, H. Zhang, Q. Zhang, Z. Huang, X. Xu, J. Guo, H. Zhang, L. Sun, Z. Zeng, A. Pan, and K. Zhang, Epitaxial nucleation and lateral growth of high-crystalline black phosphorus films on silicon, *Nat. Commun.* 11(1), 1330 (2020)
25. A. Jakhar, V. Dhyani, and S. Das, Room temperature terahertz detector based on single silicon nanowire junctionless transistor with high detectivity, *Semicond. Sci. Technol.* 35(12), 125020 (2020)
26. C. Y. Wu, W. Zhou, N. J. Yao, X. Xu, Y. Qu, Z. Zhang, J. Wu, L. Jiang, Z. Huang, and J. Chu, Silicon-based high sensitivity of room-temperature microwave and sub-terahertz detector, *Appl. Phys. Express* 12(5), 052013 (2019)
27. X. Liu, R. Singh, G. Li, C. Marques, B. Zhang, and S. Kumar, WaveFlex biosensor-using novel tri-tapered-in-

- tapered four-core fiber with multimode fiber coupling for detection of aflatoxin B₁, *J. Lightwave Technol.* 41(24), 7432 (2023)
28. X. Li, R. Singh, B. Zhang, S. Kumar, and G. Li, Ultralow-limit of detection optical fiber LSPR biosensor based on a ring laser for des- γ -carboxy prothrombin detection, *Photon. Res.* 13(3), 698 (2025)
 29. L. Duvillaret, F. Garet, and J. L. Coutaz, A reliable method for extraction of material parameters in terahertz time-domain spectroscopy, *IEEE J. Sel. Top. Quantum Electron.* 2(3), 739 (1996)
 30. X. Cheng, W. Xu, H. Wen, J. Zhang, H. Zhang, H. Li, and F. M. Peeters, Key electronic parameters of 2H-stacking bilayer MoS₂ on sapphire substrate determined by terahertz magneto-optical measurement in Faraday geometry, *Front. Phys. (Beijing)* 19(6), 63204 (2024)
 31. J. W. You, Z. H. Lan, Q. Ma, Z. Gao, Y. Yang, F. Gao, M. Xiao, and T. J. Cui, Topological metasurface: From passive toward active and beyond, *Photon. Res.* 11(3), B65 (2023)
 32. Y. X. Wang, W. D. Wu, and Z. R. Zhao, Recent progress and remaining challenges of 2D material-based terahertz detectors, *Infrared Phys. Technol.* 102(1), 103024 (2019)
 33. Q. X. Qiu and Z. M. Huang, Photodetectors of 2D materials from ultraviolet to terahertz waves, *Adv. Mater.* 33(15), 2008126 (2021)
 34. J. C. Tong, F. Suo, T. N. Zhang, Z. Huang, J. Chu, and D. H. Zhang, Plasmonic semiconductor nanogroove array enhanced broad spectral band millimetre and terahertz wave detection, *Light Sci. Appl.* 10(1), 58 (2021)
 35. A. R. Wright, X. G. Xu, J. C. Cao, and C. Zhang, Strong nonlinear optical response of graphene in the terahertz regime, *Appl. Phys. Lett.* 95(7), 072101 (2009)
 36. Q. Y. Wen, W. Tian, Q. Mao, Z. Chen, W. W. Liu, Q. H. Yang, M. Sanderson, and H. W. Zhang, Graphene based all-optical spatial terahertz modulator, *Sci. Rep.* 4(1), 7409 (2014)
 37. Q. Xiao, Q. Ma, Y. M. Ning, L. Chen, S. Liu, J. Zhang, J. W. You, and T. J. Cui, Programmable topological metasurface to modulate spatial and surface waves in real time, *Nanophotonics* 13(12), 2141 (2024)
 38. J. T. Wang, M. Zhang, Z. W. Zhou, L. Li, Q. Song, and P. Yan, Room-temperature MoTe₂/InSb heterostructure large-area terahertz detector, *Infrared Phys. Technol.* 137(1), 105190 (2024)
 39. Q. Song, W. Chen, J. C. Yang, M. Zhang, F. Gao, B. Zhang, B. Dong, P. Yan, and Y. Lu, Microgrooves array on phase-change germanium-antimony-tellurium alloys nanofilm THz detector, *IEEE Sens. J.* 23(23), 28805 (2023)
 40. Z. Z. Hu, Z. G. Liu, H. L. Zhou, et al., High-sensitivity room-temperature terahertz detector with graphene-MnBi₂Te₄ heterostructure, *Infrared Laser Eng.* 53(7), 20240137 (2024)
 41. Z. Z. Peng, M. Zhang, F. L. Gao, S. Hou, B. Zhang, and Q. Song, Magnet-enhanced droplet-shaped frequency selective terahertz detector for 6G technology, *IEEE Sens. J.* 24(19), 29978 (2024)
 42. H. Xu, C. Guo, J. Z. Zhang, W. Guo, C. N. Kuo, C. S. Lue, W. Hu, L. Wang, G. Chen, A. Politano, X. Chen, and W. Lu, PtTe₂-based type-II Dirac semimetal and its van der Waals heterostructure for sensitive room temperature terahertz photodetection, *Small* 15(52), 1903362 (2019)
 43. W. L. Guo, Z. Dong, Y. J. Xu, C. Liu, D. Wei, L. Zhang, X. Shi, C. Guo, H. Xu, G. Chen, L. Wang, K. Zhang, X. Chen, and W. Lu, Sensitive terahertz detection and imaging driven by the photothermoelectric effect in ultrashort-channel black phosphorus devices, *Adv. Sci. (Weinh.)* 7(5), 1902699 (2020)
 44. Z. W. Zhou, Q. Song, Y. F. Xu, et al., MoTe₂ microfilm terahertz detector at room temperature, in: 13th Int. Conf. Adv. Infocomm Technol (ICAIT), Yanji, China, pp 81–84 (2021)
 45. Z. Z. Peng, Q. Song, J. C. Yang, M. Zhang, S. D. Hou, B. Y. Zhang, W. Chen, and Y. Q. Lu, Magnetic field enhanced frequency-selective terahertz detection via 3D printing micro-helical stepped and MoTe₂ coated arrays, *Adv. Opt. Mater.* 13(1), 2401956 (2025)
 46. Q. Song, Z. W. Zhou, G. Y. Zhu, H. Liang, M. Zhang, B. Zhang, F. Liu, and P. Yan, Microdisk array based Weyl semimetal nanofilm terahertz detector, *Nanophotonics* 11(16), 3595 (2022)